ACS Energy LETTERS

http://pubs.acs.org/journal/aelccp

LETTER

Light- and Temperature-Modulated Magneto-Transport in Organic–Inorganic Lead Halide Perovskites

Masoumeh Keshavarz,*[,†] Steffen Wiedmann,[‡] Haifeng Yuan,[†] Elke Debroye,[†] Maarten Roeffaers,[§] and Johan Hofkens*[,†]

[†]Molecular Imaging and Photonics, Department of Chemistry, KU Leuven, Celestijnenlaan 200F, 3001 Leuven, Belgium

[‡]High Field Magnet Laboratory (HFML–EMFL), Radboud University, 6525 ED Nijmegen, Nijmegen, Netherlands

[§]Department of Molecular and Microbial Systems, KU Leuven, Kasteelpark Arenberg 23, B-3001 Heverlee, Belgium

Supporting Information

ABSTRACT: The optoelectronic properties and charge carrier dynamics in hybrid organic–inorganic perovskites under steady-state illumination are the key elements for understanding their high efficiency. We present temperature-dependent Hall and photoconductivity measurements down to a temperature of 4.2 K on single crystals of $MAPbI_3$ and $MAPbBr_3$ in magnetic fields up to 30 T and observed different transport regimes. For temperatures down to 25 K, charge transport is dominated by acoustic phonon scattering as inferred from the temperature dependence of both zero and high-field resistance. Below 25 K, transport is determined by thermally activated hopping of charge carriers reflected in a diverging zero-field resistance and a strong decrease in the carrier's mobility and concentration. Our findings demonstrate the importance of performing experiments at low temperature to unravel the fundamental charge carrier dynamics and stimulate the need for a comprehensive theoretical model for perovskite-based devices.

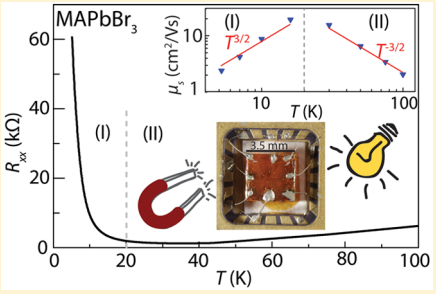

High energy conversion efficiency in combination with a low-cost production makes hybrid organic–inorganic perovskites ideal for photovoltaic applications.[1−3] The superior device performance of this class of materials is associated with a high absorption coefficient,[4] low exciton binding energies,[5−8] and extended carrier lifetimes and diffusion lengths of photogenerated charge carriers. Recently it has been shown in $MAPbI_3$ ($MA = CH_3NH_3^+$) that this extended carrier lifetime originates from a slow, thermally activated recombination process due to the mixed direct–indirect character of the band structure.[9] The intrinsic photophysical parameters such as carrier mobility, charge diffusion, and recombination dynamics have been investigated indirectly by fast spectroscopic techniques.[10−13] However, these techniques probe carrier dynamics at short time scales after absorption of the incident photons in contrast to perovskite-based optoelectronic devices operating under steady-state illumination. Therefore, it is crucial to perform transport measurements under steady illumination to determine the fundamental photophysical properties and to identify the intrinsic scattering mechanisms on impurities, defects, and phonons at low temperatures when the thermal energy becomes negligible to unravel the superior device performance of these materials. To date, steady-state photoluminescence experiments have established that the Fröhlich interaction between longitudinal optical phonons and charge carriers is the dominant contribution at room temperature.[14] However, there is no clear picture describing which mechanisms are dominant at different temperatures, in particular to distinguish the charge carrier interaction with optical and acoustic phonons. Moreover, organic–inorganic lead halide perovskites undergo structural phase transitions with decreasing temperature, potentially altering the charge carrier properties due to the coupling between structural fluctuations and electronic properties. $MAPbI_3$ exhibits two phases below room temperature: a tetragonal phase ($I4/mcm$) from 293 to 160 K followed by an orthorhombic ($Pnma$) phase below 160 K.[15] $MAPbBr_3$ is in the cubic phase ($Pm3m$) down to 237 K and then exhibits two tetragonal phases between 155 and 150 K ($I4/mcm$ and $P4/mmm$) followed by an orthorhombic phase ($Pna2_1$) below 144 K.[15]

In this Letter, we present a temperature-dependent Hall and magneto-resistance study under steady-state illumination in bulk single crystals of $MAPbBr_3$ and $MAPbI_3$. This method allows us to directly access the photogenerated charge carrier concentration and mobility. From the temperature-dependent

Received: September 28, 2017
Accepted: November 20, 2017
Published: November 20, 2017

DOI: 10.1021/acsenergylett.7b00941
ACS Energy Lett. 2018, 3, 39−45

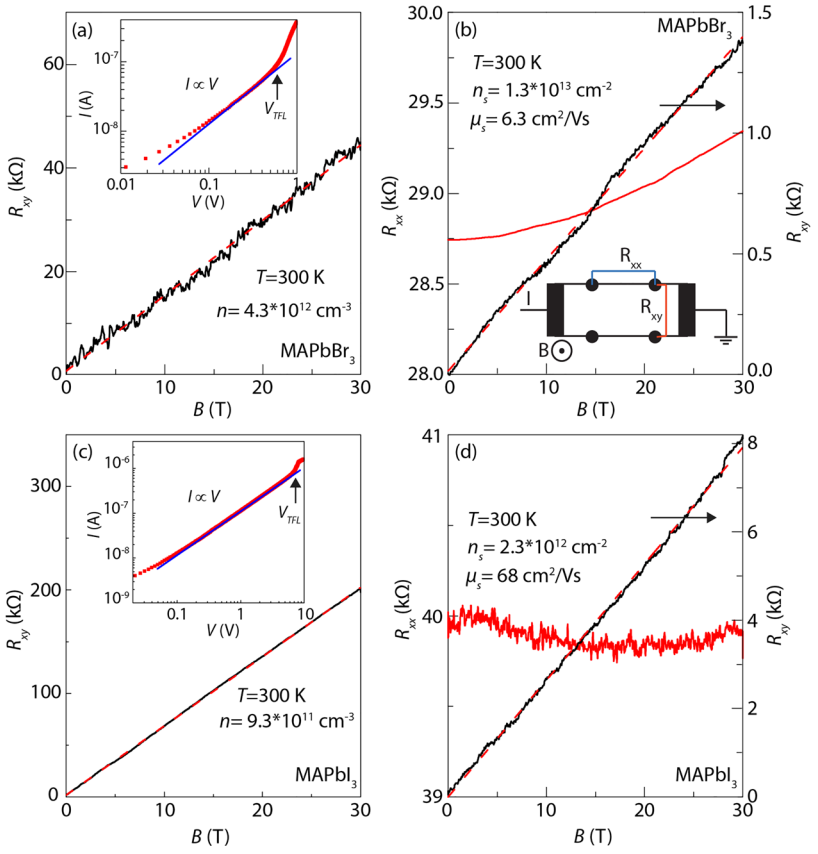

Figure 1. Room-temperature magneto-transport in $MAPbBr_3$ and $MAPbI_3$. (a) Hall resistance R_{xy} as a function of the magnetic field B (inset: $I-V$ characteristics; the ohmic regime is indicated by the blue line; V_{TFL} = 0.45 V) for $MAPbBr_3$ in the dark. (b) R_{xy} and R_{xx} as a function of B under steady-state illumination for $MAPbBr_3$ (inset: schematic representation of the device configuration used for measurements). (c) R_{xy} as a function of B (inset: $I-V$ characteristics; ohmic regime see blue line; V_{TFL} = 6.2 V) for $MAPbI_3$ in the dark. (d) R_{xy} and R_{xx} as a function of B under steady-state illumination for $MAPbI_3$. The extracted transport parameters n, n_s, and μ_s are indicated in each plot.

study of the zero and high-field resistance, we unambiguously identify distinct transport regimes. In the orthorhombic phase, between 100 and 25 K where a maximum in the charge carrier mobility is found, transport is governed solely by scattering with acoustic phonons evident from the temperature dependence of the carrier mobility ($\mu_s \propto T^{-3/2}$). Below 25 K, we observe an exponential increase in the resistance accompanied by a strong decrease in the charge carrier concentration which is attributed to thermally activated hopping of charge carriers.

We first present the sample characterization for both $MAPbBr_3$ and $MAPbI_3$ single crystals at 300 K in Figure 1. These single crystals have been used to make devices on which four or six electrodes have been evaporated (see inset to Figure 1b). The magnetic field B is applied perpendicular to the device (see Experimental Methods). Prior to transport experiments, the current−voltage ($I-V$) characteristics of each device are probed in dark conditions to determine the ohmic regime (blue line) as shown in the inset of Figure 1a for $MAPbBr_3$ and Figure 1c for $MAPbI_3$. Above a threshold voltage, the $I-V$ curves deviate from the ohmic regime for both devices, and the trap-filled regime is reached.[11,16,17] From the trap-filled limit voltage, V_{TFL}, and the dielectric constants, ε (25.5 for $MAPbBr_3$[15] and ∼30 for $MAPbI_3$[15,17]), the trap density $n_t = 2V_{TFL}\varepsilon\varepsilon_0/(ed^2)$ (d is the material's thickness) is calculated to be $n_t = 1.3 \times 10^9$ cm^{-3} for $MAPbBr_3$ and $n_t = 2.1 \times 10^{10}$ cm^{-3} for $MAPbI_3$, in agreement with the literature.[11] The Hall resistance R_{xy} in dark for both materials, see Figure 1a,c, depends linearly on B up to 30 T. From the slope of R_{xy}, a bulk carrier concentration of $n = 4.3 \times 10^{12}$ cm^{-3} for $MAPbBr_3$ and $n = 9.3 \times 10^{11}$ cm^{-3} for $MAPbI_3$ is extracted, in agreement with the values reported in the literature.[10,11,18−22]

The transport properties of the devices alter under steady state illumination (2 mW, λ = 373 nm). In all photoconductivity measurements, the incident photon energy (E_λ = 3.3 eV) is larger than the band gap E_g (E_g = 2.2 eV $MAPbBr_3$, E_g = 1.5 eV $MAPbI_3$[15]), therefore generating electron−hole pairs via photon absorption. Using the continuity equation for photoconduction dynamics in the steady-state case, see the Supporting Information,[23] electron−hole recombination (bimolecular decay) is identified as the dominant mechanism at the photoexcitation power used in our experiment in agreement with other measurements in bulk single crystals[20] and in thin perovskite films.[20,24,25]

In Figure 1b,d, the transverse resistance R_{xx} and R_{xy} are plotted as a function of B at T = 300 K. R_{xy} shows a linear increase in B, and from its slope, a sheet carrier concentration of $n_s = 1.3 \times 10^{13}$ cm^{-2} for $MAPbBr_3$ and $n_s = 2.3 \times 10^{12}$ cm^{-2} for $MAPbI_3$ is extracted. Throughout this Letter, the term sheet carrier concentration n_s is employed for the bulk device under steady-state illumination because the absorption length is much smaller than the thickness of the crystals. An effective bulk carrier concentration under light taking into account the carrier lifetime and diffusion length is presented in the Supporting Information.[23] The observed linearity in R_{xy} even up to 30 T in the dark and under illumination indicates that charge transport is dominated by one type of charge carrier. From the extracted

DOI: 10.1021/acsenergylett.7b00941
ACS Energy Lett. 2018, 3, 39−45

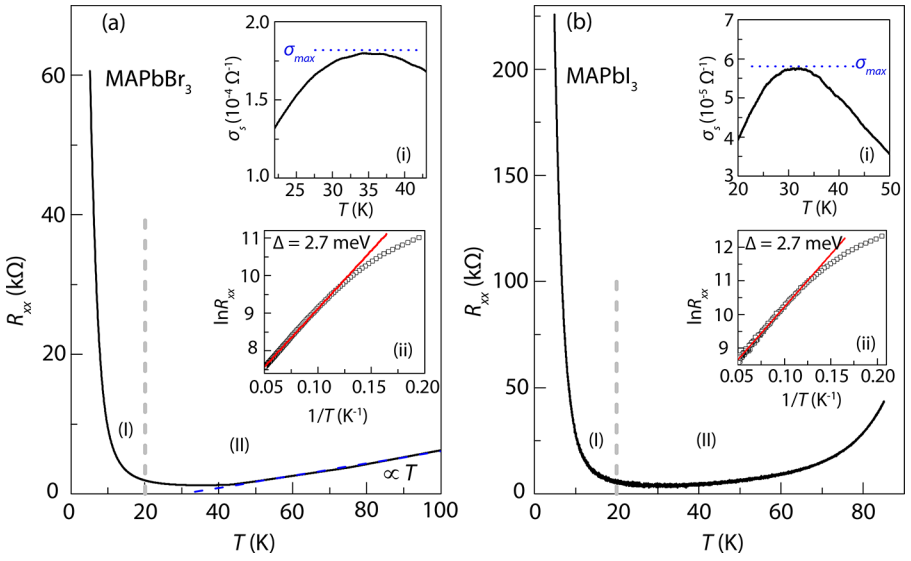

Figure 2. Temperature-dependent zero-field resistance in the orthorhombic phase for $MAPbBr_3$ and $MAPbI_3$ under steady state illumination. (a, b) Temperature dependence of the longitudinal resistance R_{xx} between 4.2 and 100 K. We identify two regimes with increasing T: Regime I is governed by thermally activated hopping transport; the gaps are indicated in each figure inset (ii). Regime II is characterized by a very low resistance in which the minimum of R_{xx} can be found, and in which R_{xx} increases seemingly linear in T, more pronounced for $MAPbBr_3$. Inset i highlights the region of maximum sheet conductivity σ_s in regime II, and inset ii shows the extraction of the energy gap Δ in regime I.

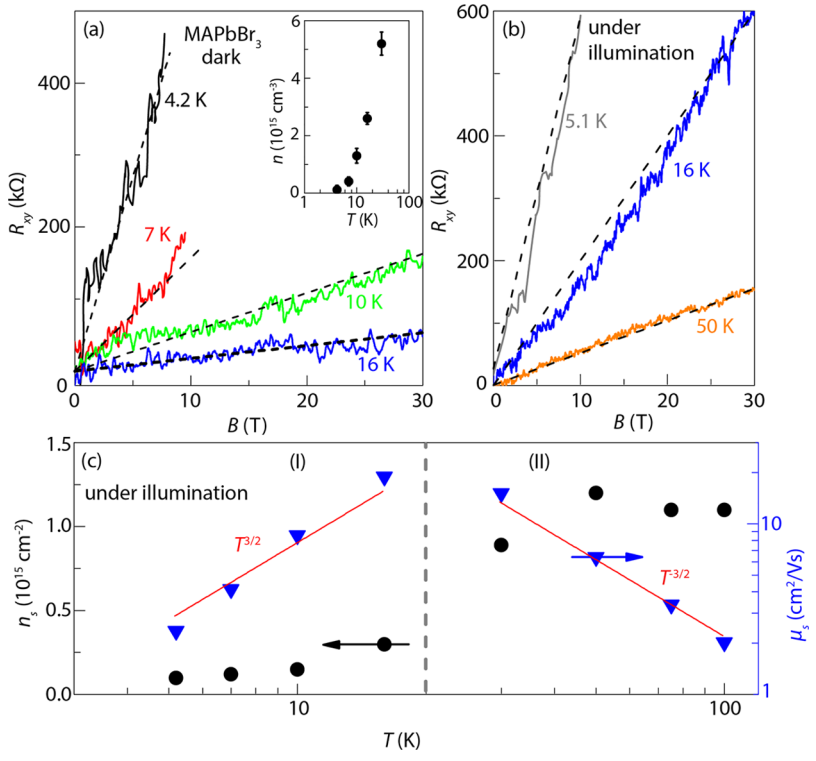

Figure 3. Temperature-dependent Hall resistance R_{xy}, sheet carrier concentration n_s, and mobility μ_s for $MAPbBr_3$. (a) R_{xy} for several chosen temperatures in the dark. The black dashed lines show the range of the linear fit. The inset shows the carrier concentration as a function of temperature. (b) R_{xy} under illumination at 5.1, 16, and 50 K. (c) Temperature-dependence of the carrier concentration and mobility under illumination from 4.2 to 100 K. n_s increases by an order of magnitude from 4.2 to 50 K and then saturates above 50 K. μ_s first increases with $T^{3/2}$ and has its maximum at 16 K with μ_s = 20 $cm^2/(V\,s)$ but then decreases with $T^{-3/2}$ because of scattering with acoustic phonons.

sheet carrier concentrations and the zero-field resistivity ρ_{xx}, taking into account the device geometry (see Experimental Methods), we find a carrier mobility of μ_s = 6.3 $cm^2/(V\,s)$ for $MAPbBr_3$ and μ_s = 68 $cm^2/(V\,s)$ for $MAPbI_3$, under steady-state illumination. This mobility is in the order of magnitude as reported in ref 20 and by roughly 2 orders of magnitude smaller than the electron mobility in conventional inorganic semiconductors such as Si or GaAs and thereby is not a hindrance in terms of their power conversion efficiency.[26] The transverse resistance R_{xx} as a function of the magnetic field is shown in Figure 1b,d for both materials up to 30 T under illumination. We observe a slight increase in R_{xx} for $MAPbBr_3$ due to classical

DOI: 10.1021/acsenergylett.7b00941
ACS Energy Lett. 2018, 3, 39−45

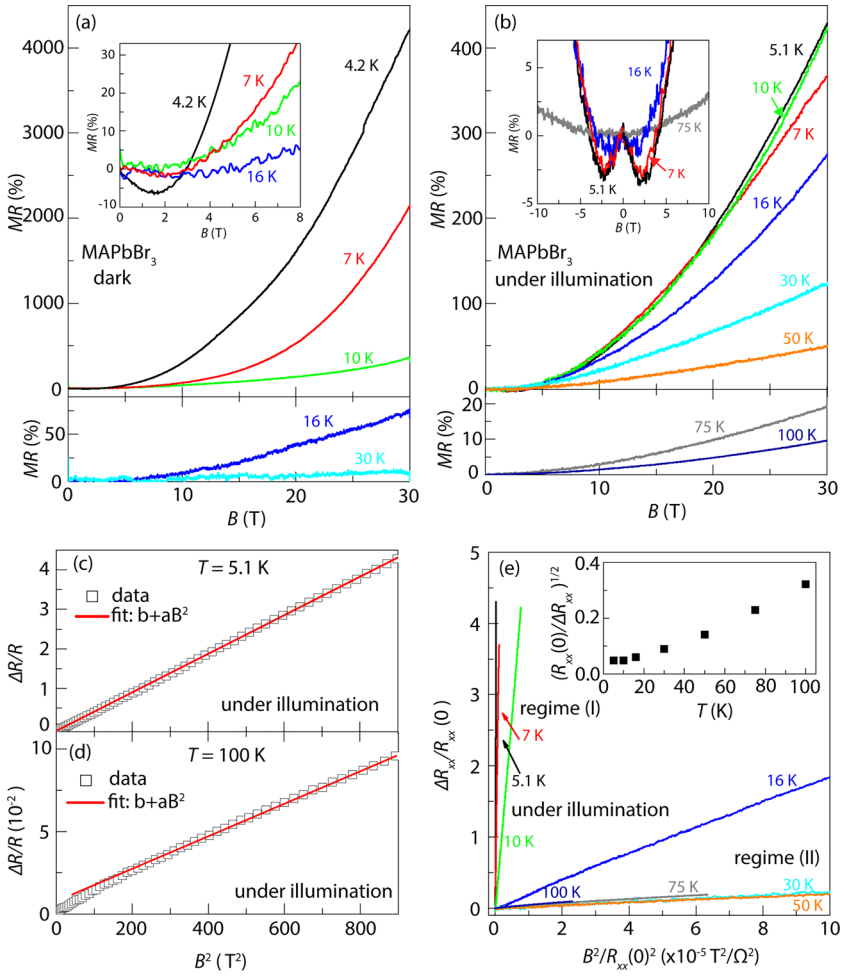

Figure 4. Investigation of the magneto-resistance in the orthorhombic regime for $MAPbBr_3$. (a) MR in the dark at 4.2, 7, 10, 16, and 30 K and (b) MR under illumination for different temperatures from 5.1 to 100 K. For all temperatures we observe an overall positive quadratic high-field MR that is suppressed with increasing temperature. The insets show a zoom into the low-field region where a negative MR is observed at low T that gradually disappears with increasing T. (c, d) $\Delta R_{xx}/R_{xx}(0)$ as a function of B^2 under light at 5.1 and 100 K: the straight red line indicates the regime where $\Delta R_{xx}/R_{xx}(0)$ is proportional to B^2. (e) Kohler plot for the MR under illumination. All the curves merge together above T = 30 K. Inset: Temperature dependence of $(R_{xx}(0)/\Delta R_{xx})^{1/2}$ at 30 T as a function of temperature under illumination.

orbital effects, whereas the R_{xx} does not change significantly for $MAPbI_3$.

We now focus on transport experiments for T < 100 K under steady-state illumination. Figure 2 depicts typical curves for R_{xx} at B = 0 as a function of temperature T in $MAPbBr_3$ (Figure 2a) and $MAPbI_3$ (Figure 2b). Both materials exhibit qualitatively similar temperature dependence which can be divided in two regimes. With decreasing temperature below 100 K, R_{xx} decreases ($dR/dT > 0$) until a saturation is reached around 35 K resembling a purely metallic behavior that can be attributed to electron−phonon scattering.[27] For $MAPbBr_3$, this decrease is linear as a function of T from 100 to 40 K as indicated by the dashed blue line. We find the highest sheet conductivity of $\sigma_s = 1.8 \times 10^{-4}$ 1/Ω at T = 35 K for $MAPbBr_3$ and $\sigma_s = 5.8 \times 10^{-5}$ 1/Ω at T = 32 K for $MAPbI_3$ (see inset i in Figure 2).

Regime I, T < 20 K, is characterized by an exponential increase in R ($dR/dT < 0$) for both devices in which R_{xx} increases by roughly 2 orders of magnitude compared to regime II. Hence, this regime is dominated by thermally activated hopping of electrons that are bound in traps resulting from impurities and defects that can be associated with an average energy Δ. Thermal activation in the order of Δ leads to a charge carrier conductivity which is proportional to $\exp(-\Delta/k_BT)$, where k_B is the Boltzmann constant. In Figure 2a,b, inset ii, we extract Δ = 2.7 meV for $MAPbBr_3$ and $MAPbI_3$, indicated by the dashed line.

We then explore the transport parameters in the orthorhombic phase between 4.2 and 100 K. In Figure 3a,b, the Hall resistance R_{xy} for $MAPbBr_3$ at different temperatures in the dark and under steady-state illumination is illustrated. Data for $MAPbI_3$ are shown in the Supporting Information in Figure S3. Without illumination, the Hall resistance is linear in B, and from the low-field R_{xy}, we extract n, which is plotted as a function of temperature in the inset of Figure 3a. We find that the carrier concentration strongly decreases with decreasing temperature from 30 K ($n = 5.2 \times 10^{15}$ cm^{-3}) to 4.2 K ($n = 1.2 \times 10^{14}$ cm^{-3}). The linear Hall resistance R_{xy} under illumination as a function of B is presented in Figure 3b for T = 5.1, 16, and 50 K. In Figure 3c, we plot n_s, extracted from the slope of R_{xy}, and the carrier mobility μ_s, obtained from the temperature dependence of the zero-field resistivity, as a function of temperature. n_s increases by an order of magnitude from 4.2 to 50 K and then saturates around $n_s = 1.2 \times 10^{15}$ cm^{-2} for T > 50 K. At the same time, μ_s first increases ($\mu_s \sim T^{3/2}$, indicated by the straight red line) with increasing temperature

DOI: 10.1021/acsenergylett.7b00941
ACS Energy Lett. 2018, 3, 39−45

and has its maximum at 16 K (μ_s = 20 cm^2/(V s)). We note that a $T^{3/2}$ dependence of the carrier mobility is reminiscent of charged impurity scattering in semiconductors.[27] For T > 25 K, μ_s decreases with increasing temperature ($\mu_s \propto T^{-3/2}$, straight line) which is the regime where charge carrier scattering is dominated by acoustic phonons.

Next, we focus on the emergence of a large magneto-resistance (MR) in organic−inorganic lead halide perovskites in the orthorhombic regime, which is an independent probe to determine the underlying scattering mechanisms of charge carriers. The MR is defined as MR = $[R_{xx}(B) - R_{xx}(0)]/R_{xx}(0) = \Delta R_{xx}/R_{xx}(0)$, where $R_{xx}(B)$ is the resistance in the presence of a magnetic field B.

In nonmagnetic materials as hybrid perovskites, the transverse MR is proportional to B^2 for $B \rightarrow \infty$, see for example ref 27. Figure 4 illustrates the observation of a large MR in $MAPbBr_3$. Data for $MAPbI_3$ are shown in the Supporting Information in Figure S4. In Figure 4a,b, we show the MR at different temperatures up to 30 T without and under steady-state illumination. The MR at 30 T reaches 4000% in dark and 400% under illumination. Moreover, the MR in the presence of steady-state illumination exhibits the B^2-dependence, see Figure 4c,d at 5.1 and 100 K (red line) reflecting the classical MR behavior in the case of open orbits.[27,28]

The MR is strongly suppressed with increasing temperature as illustrated in Figure 4a. At 30 T and 30 K, the MR is 12% in the dark and 120% under illumination. With increasing temperature, the MR under illumination is also gradually suppressed (10% at 100 K). Interestingly, at low temperature (4.2 K), we find that the MR is first decreasing for B < 1.5 T and then turns into a strongly positive and quadratic MR. As the temperature increases, this negative low-field MR becomes weaker and the onset of quadratic MR shifts to higher magnetic field values (see inset to Figure 4a). This negative MR at low B is also present under illumination and remains more pronounced at higher temperature compared to the MR in dark (see inset to Figure 4b). In contrast, the crossover from a negative MR to a positive MR under illumination gradually shifts toward lower magnetic fields with increasing temperature. This low-field negative MR occurs solely in regime I and is attributed to a field-enhanced conductivity in the thermally activated hopping transport regime due to an increase in the effective mean free path of the carriers in the presence of a small magnetic field.

Measuring resistivity at different temperatures and plotting MR as a function of magnetic field normalized by the zero-field resistance results in a temperature-independent curve referred to as Kohler plot, in which all MR curves that are governed by the same scattering mechanisms merge. Figure 4e illustrates such a Kohler plot for the MR for the data presented in Figure 4b as a function of B^2 normalized by $R_{xx}(0)^2$. As inferred from the temperature dependence of the zero-field resistivity (Figure 2) for T > 30 K, we clearly see that all isotherms of magneto-resistance are dominated by one scattering mechanism which has been identified as scattering of acoustic phonons in Figure 3c. Next, we plot the square root of the inverse MR, $(R_{xx}(0)/\Delta R_{xx})^{1/2}$, which is proportional to the scattering rate $1/\tau$, as a function of the temperature at 30 T (see inset to Figure 4e). For T > 30 K, the linear increase in $(R_{xx}(0)/\Delta R_{xx})^{1/2}$ with increasing T also suggests that electron−phonon scattering is the dominant scattering mechanism in this regime.[27]

Using magneto-transport under steady-state illumination, we have determined the temperature-dependent photophysical properties and identified the electron−acoustic phonon scattering as the dominant scattering in single crystals of $MAPbBr_3$ and $MAPbI_3$. Our work paves the way towards exploring more advanced groups of perovskites or complex devices such as thin-film field-effect transistors ultimately leading to the development of the next-generation devices.

EXPERIMENTAL METHODS

Device Synthesis and Characterization. The bulk single crystals with flat facets up to 4 × 4 mm^2 and a thickness of 1 mm were grown using the inverse temperature crystallization (ITC) method as reported in the literature.[16] As-grown crystals with a regular shape have been chosen for the experiments, and a small amount of Au has been evaporated (in vacuum) on the sample edges, either in a four-terminal, eight-terminal, or Hall-bar configuration. The sample preparation has been carried out under ambient conditions. Au wires with a diameter of 25 μm have been attached by means of Ag conductive paste to the device which we mounted on a chip carrier. The contact resistances (two-terminal resistances) were above 40 MΩ in the dark and hundreds of kilo-ohms to a few megaohms under monochromatic illumination. Prior to the transport experiments, we measured $I-V$ curves of the contacts pairs (see insets to Figures 1a,c).

Magneto-Transport Experiments. A special probe that is equipped with an optical fiber, a calibrated Cernox thermometer, and a strain gauge heater has been employed. For the transport experiments, the sample in the chip carrier has been mounted under ambient conditions in the probe that has been put in a vacuum tube equipped with an additional inner vacuum chamber (IVC) to perform transport experiments between 4.2 and 300 K. In the vacuum tube, the sample was either kept in the dark or has been illuminated with monochromatic light. The vacuum tube and the IVC has been evacuated at room temperature (<10^{-5} mbar). After pumping, a small amount of ^{4}He contact gas has been added to the vacuum tube to ensure a thermal equilibrium for the temperature-dependent measurements from 300 to 4.2 K (these were the conditions throughout the entire experiments). The vacuum tube has then been put in a cryostat for the experiments at low temperatures and high magnetic fields. The temperature was controlled and stabilized using a standard Lakeshore temperature controller. The DC measurements have been performed using a Keithley 6221 current source, and the DC voltage has been recorded by standard (nano)voltmeters (Keithley 2000 or 2184). For the AC measurements, the same current source at frequencies around 13 Hz and Stanford 830 Lock-in amplifiers with suitable preamplifiers were employed. The applied excitation current was in the range between 10 nA and 1 μA (always in the ohmic regime). A solid-state laser (373 nm) was utilized for the photoconductivity measurements. Each power has been measured using a standard power meter prior to device exposure. For the light intensity (illumination source intensity) used in our experiments, a saturation of the photoconductivity has been observed within a few seconds to roughly 10 s. Once the photoconductivity was constant, we performed the resistance and Hall measurements as a function of magnetic field or temperature.

For the experiments in a magnetic field, either a 15 T superconducting magnet or a 33 T Bitter magnet with a 32 mm room-temperature bore was used. The magnetic field was oriented always perpendicular to the current along the c-axis. We measure the transverse resistance R_{xx} (transverse magneto-

DOI: 10.1021/acsenergylett.7b00941
ACS Energy Lett. 2018, 3, 39−45

resistance) and Hall resistance R_{xy} in the direction perpendicular to the magnetic field B (i.e., both the applied current and the electric field are in the plane perpendicular to the magnetic field B).

The resistivity ρ_{xx} of the devices (van der Pauw geometry) was extracted from the measured resistance R_{xx} using the method as described in ref 29. In a device with four contacts, both Hall configurations have been measured. For all resistance or resistivity curves presented, R_{xx} (R_{xy}) has been measured for both positive and negative magnetic fields, and the data have been symmetrized (antisymmetrized). In the Supporting Information, we have employed a six-terminal $MAPbI_3$ device in Hall-bar geometry.

■ ASSOCIATED CONTENT

Supporting Information

The Supporting Information is available free of charge on the ACS Publications website at DOI: 10.1021/acsenergylett.7b00941.

Estimation of the effective bulk carrier concentration (n_b) of the crystals under steady-state illumination, carrier lifetime (τ), and diffusion length (l_d); additional transport data on a bulk single crystal of $MAPbI_3$; and optical characterization measurements at room temperature (PDF)

■ AUTHOR INFORMATION

Corresponding Authors

*E-mail: masoumeh.keshavarz@kuleuven.be.
*E-mail: johan.hofkens@kuleuven.be.

ORCID

Masoumeh Keshavarz: 0000-0003-3685-6778
Haifeng Yuan: 0000-0001-6652-3670
Johan Hofkens: 0000-0002-9101-0567

Notes

The authors declare no competing financial interest.

■ ACKNOWLEDGMENTS

We acknowledge financial support from the Research Foundation-Flanders (FWO, Grant G 0683.15, GOA5817.N, large infrastructure grant ZW15_09 GOH6316N, postdoctoral fellowship to E.D., H.Y. and M.K. (FWO Grant 12Y6418N)), the Flemish government through long-term structural funding Methusalem (CASAS2, Meth/15/04), the Hercules Foundation (HER/11/14), the Belgian Federal Science Policy Office (IAP-PH05), and the EC through the Marie Curie ITN project iSwitch (GA-642196). We acknowledge enlightening discussions with Nigel Hussey. The support of the HFML-RU/FOM, member of the European Magnetic Field Laboratory (EMFL), is also acknowledged.

■ REFERENCES

(1) Green, M. A.; Ho-Baillie, A.; Snaith, H. J. The emergence of perovskite solar cells. *Nat. Photonics* **2014**, *8*, 506−514.
(2) Jeon, N. J.; Noh, J. H.; Yang, W. S.; Kim, Y. C.; Ryu, S.; Seo, J.; Seok, S. I. Compositional engineering of perovskite materials for high-performance solar cells. *Nature* **2015**, *517*, 476−480.
(3) Green, M. A.; Emery, K.; Hishikawa, Y.; Warta, W.; Dunlop, E. D. Solar cell efficiency tables (version 45). *Prog. Photovoltaics* **2015**, *23*, 1−9.
(4) Lee, M. M.; Teuscher, J.; Miyasaka, T.; Murakami, T. N.; Snaith, H. J. Efficient hybrid solar cells based on meso-superstructured organometal halideperovskites. *Science* **2012**, *338*, 643−647.
(5) D'Innocenzo, V.; Grancini, G.; Alcocer, M. J. P.; Kandada, A. R. S. K.; Stranks, S. D.; Lee, M. M.; Lanzani, G.; Snaith, H. J.; Petrozza, A. Excitons versus free charges in organo-lead tri-halide perovskites. *Nat. Commun.* **2014**, *5*, 3586.
(6) Herz, L. M. Charge carrier dynamics in organic-inorganic metal halide perovskites. *Annu. Rev. Phys. Chem.* **2016**, *67*, 65.
(7) Fang, H.-H.; Raissa, R.; Abdu-Aguye, M.; Adjokatse, S.; Blake, G. R.; Even, J.; Loi, M. A. Photophysics of Organic−inorganic Hybrid Lead Iodide Perovskite Single Crystals. *Adv. Funct. Mater.* **2016**, *25*, 2378−2385.
(8) Miyata, A.; Mitioglu, A.; Plochocka, P.; Portugall, O.; Wang, J. T.-W.; Stranks, S. D.; Snaith, H. J.; Nicholas, R. J. Direct Measurement of the Exciton Binding Energy and Effective Masses for Charge Carriers in an Organic-inorganic Tri-halide Perovskite. *Nat. Phys.* **2015**, *11*, 582−587.
(9) Hutter, E. M.; Gélvez-Rueda, M. C.; Osherov, A.; Bulović, V.; Grozema, F. C.; Stranks, S. D.; Savenije, T. J. Direct−indirect character of the bandgap in methylammonium lead iodide perovskite. *Nat. Mater.* **2017**, *16*, 115−120.
(10) Wehrenfennig, C.; Eperon, G. E.; Johnston, M. B.; Snaith, H. J.; Herz, L. M. High Charge Carrier Mobilities and Lifetimes in Organolead Trihalide Perovskites. *Adv. Mater.* **2014**, *26*, 1584.
(11) Shi, D.; et al. Low trap-state density and long carrier diffusion in organolead trihalide perovskite single crystals. *Science* **2015**, *347*, 519−522.
(12) Bi, Y.; Hutter, E. M.; Fang, Y.; Dong, Q.; Huang, J.; Savenije, T. J. Charge Carrier Lifetimes Exceeding 15 μs in Methylammonium Lead Iodide Single Crystals. *J. Phys. Chem. Lett.* **2016**, *7* (5), 923−928.
(13) Mante, P.-A.; Stoumpos, C. C.; Kanatzidis, M. G.; Yartsev, A. Electron-acoustic phonon coupling in single crystal $Ch_3NH_3PbI_3$ perovskites revealed by coherent acoustic phonons. *Nat. Commun.* **2017**, *8*, 14398.
(14) Wright, A. D.; Verdi, C.; Milot, R. L.; Eperon, G. E.; Pérez-Osorio, M. A.; Snaith, H. J.; Giustino, F.; Johnston, M. B.; Herz, L. M. Electron−phonon coupling in hybrid lead halide perovskites. *Nat. Commun.* **2016**, *7*, 11755.
(15) Poglitsch, A.; Weber, D. Dynamic disorder in methylammonium trihalogenplumbates (II) observed by millimeter-wave spectroscopy. *J. Chem. Phys.* **1987**, *87*, 6373−6378.
(16) Saidaminov.; et al. High-quality bulk hybrid perovskite single crystals within minutes by inverse temperature crystallization. *Nat. Commun.* **2015**, *6*, 7586.
(17) Dong, Q.; Fang, Y.; Shao, Y.; Mulligan, P.; Qiu, J.; Cao, L.; Huang, J. Electron-hole diffusion lengths > 175 μm in solution-grown $CH_3NH_3PbI_3$ single crystals. *Science* **2015**, *347*, 967−970.
(18) Mitzi, D. B.; Feild, C. A.; Schlesinger, Z.; Laibowitz, R. B. Transport, opticaland magnetic properties of the conducting halide perovskite $CH_3NH_3SnI_3$. *J. Solid State Chem.* **1995**, *114*, 159−163.
(19) Johnston, M. B.; Herz, L. M. Hybrid perovskites for photovoltaics: Charge-carrier recombination, diffusion, and radiative efficiencies. *Acc. Chem. Res.* **2016**, *49*, 146−154.
(20) Chen, Y.; Yi, H. T.; Wu, X.; Haroldson, R.; Gartstein, Y. N.; Rodionov, Y. I.; Tikhonov, K. S.; Zakhidov, A.; Zhu, X.-Y.; Podzorov, V. Extended carrier lifetimes and diffusion in hybrid perovskites revealed by Hall effect and photoconductivity measurements. *Nat. Commun.* **2016**, *7*, 12253.
(21) Yi, H. T.; Wu, X.; Zhu, X.; Podzorov, V. Intrinsic Charge Transport across Phase Transitions in Hybrid Organo-Inorganic Perovskites. *Adv. Mater.* **2016**, *28*, 6509−6514.
(22) Senanayak, S. P.; et al. Understanding charge transport in lead iodide perovskite thin-film field-effect transistors. *Science Advances* **2017**, *3*, e1601935.
(23) The Supporting Information includes a discussion on photoconduction dynamics, the device characterization under steady-state illumination, measurements on a $MAPbI_3$ device, and optical characterization.

DOI: 10.1021/acsenergylett.7b00941
ACS Energy Lett. 2018, 3, 39−45

(24) Stranks, S. D.; Burlakov, V. M.; Leijtens, T.; Ball, J. M.; Goriely, A.; Snaith, H. J. Recombination Kinetics in Organic-Inorganic Perovskites: Excitons, Free Charge,and Subgap States. *Phys. Rev. Appl.* **2014**, *2*, 034007.
(25) Sveinbjornsson, K.; Aitola, K.; Zhang, X.; Pazoki, M.; Hagfeldt, A.; Boschloo, G.; Johansson, E. M. J. J. *J. Phys. Chem. Lett.* **2015**, *6*, 4259−4264.
(26) Brenner, T. M.; Egger, D. A.; Rappe, A. M.; Kronik, L.; Hodes, G.; Cahen, D. Are Mobilities in Hybrid Organic-Inorganic Halide Perovskites Actually "High"? *J. Phys. Chem. Lett.* **2015**, *6*, 4754.
(27) Singleton, J. *Band Theory and Electronic Properties of Solids*; Oxford Master Series in Condensed Matter Physics; University Press: Oxford, UK, 2001.
(28) Rossiter, P. L.; Bass, J. Electronic Transport Properties of Normal Metals. *Mater. Sci. Technol.*, **2006**. DOI: 10.1002/9783527603978.mst0033.
(29) van der Pauw, L. J. A Method of Measuring Specific Resistivity and Hall Effect of Discs of Arbitrary Shape. *Philips Res. Rep.* **1958**, *13*, 1−9.

DOI: 10.1021/acsenergylett.7b00941
ACS Energy Lett. 2018, 3, 39−45